Current Generation Mechanism in Self-assembled Electret-based Vibrational Energy Generators

Yuya Tanaka,[1,2,3]* Noritaka Matsuura,[2] and Hisao Ishii[1,2,4]

[1]Center for Frontier Science, Chiba University, 1-33 Yayoi-cho, Inage-ku, Chiba 263-8522, Japan
[2]Graduate School of Science and Engineering, Chiba University, 1-33 Yayoi-cho, Inage-ku, Chiba 263-8522, Japan
[3]Japan Science and Technology Agency, PRESTO, 4-1-8 Hon-cho, Kawaguchi 332-0012, Japan
[4]Molecular Chirality Research Center, Chiba University, 1-33 Yayoi-cho, Inage-ku, Chiba 263-8522, Japan

Electret-based vibrational energy generators (E-VEGs) have attracted considerable attention because they can generate electrical power from ambient vibration. E-VEGs have a capacitor structure in which an electret and air gap are sandwiched by electrodes, and the devices are automatically charged by the electric field of the electret. Although various charging processes for dielectric materials to be polarized have been proposed, they lead to low productivity of the device. Recently, we have developed a self-assembled electret (SAE)-based VEG that does not require any charging process. The SAE was realized by utilizing the spontaneous orientation of polar molecules for organic light-emitting diodes: positive and negative polarization charges exist on the film surface and reverse side. Because an electric field will not be formed outside of the SAE, the driving force inducing charge carriers on the electrodes of the SAE-VEG has not been clarified. To clarify the operation mechanism of the SAE-VEG, in this study, the relationship between the surface potential of the SAE and the current generated by electrode vibration in the SAE-VEG is carefully examined. The surface potential is changed over a wide range from negative to positive by controlling the molecular orientation. In addition to establishing a model for the device operation, we demonstrated that the output power of the SAE-VEG can be easily enhanced simply by increasing the thickness of the SAE.

1. Introduction

Vibrational energy generators (VEGs) have been extensively studied as a next-generation independent power source because they can generate electrical power from vibration, which is widely available in both residual areas and natural environments.[1–4] In particular, electret-based VEGs (E-VEGs) are interesting since they can be easily miniaturized by using fabrication processes for micro-electro-mechanical systems (MEMS).[5] E-VEGs have a capacitor structure in which the electret and air gap are sandwiched by vibrational and fixed electrodes, as shown in Fig. 1(a). Here, the electret is a dielectric material with quasi-permanent electrical charge or

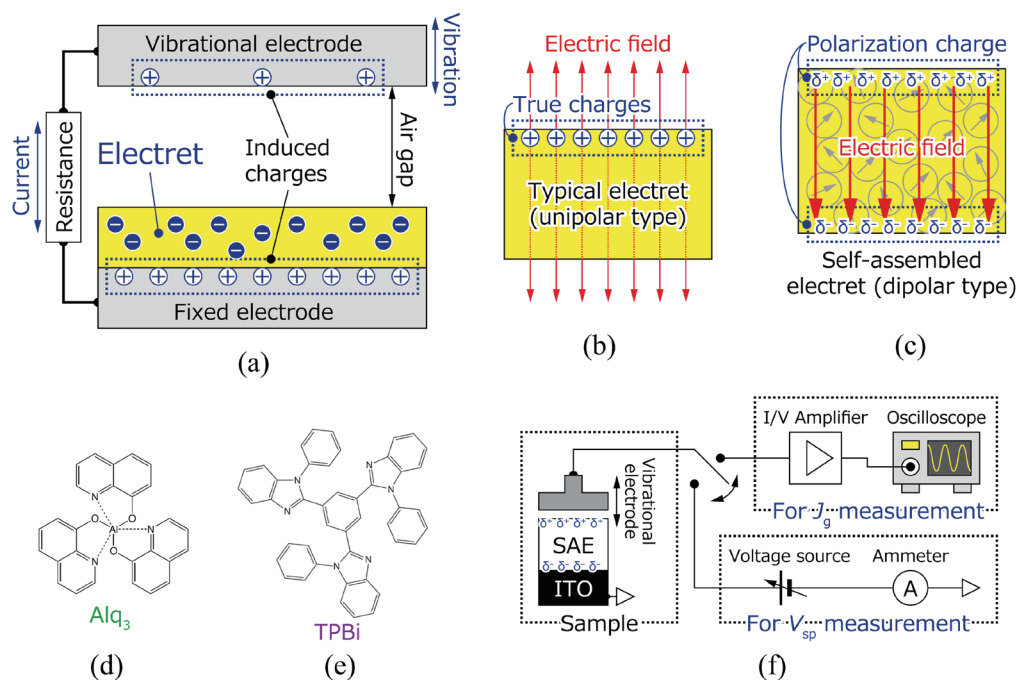*Corresponding author: e-mail: y-tanaka@chiba-u.jp

Fig. 1. (Color online) (a) Device structure of E-VEG. (b), (c) Schematic illustrations of typical electret (unipolar type) and SAE (dipolar type), respectively. (d), (e) Chemical structures of Alq$_3$ and TPBi, respectively. (f) Measurement setup for V_{sp} of the SAE and J_g in the SAE-VEG.

dipolar polarization,[6] and the E-VEGs are automatically charged by the electric field formed by the electret. The surface charges of the electret play an essential role in developing E-VEGs with high output power. Thus, various charging techniques for dielectric materials, such as corona charging, contact electrification, thermal charging, and electron- or ion-beam charging, have been proposed.[6] Furthermore, soft X-ray photoionization and ion implantation have also attracted attention because of their high compatibility with MEMS technology.[7–11] Among these techniques, corona charging is one of the most widely used charging methods, leading to the formation of the electric field [Fig. 1(b)]; however, it also involves a factor that limits the productivity of E-VEGs, as is the case with other charging techniques.

To overcome this problem, we proposed the utilization of a self-assembled electret (SAE) for E-VEGs.[12] A notable advantage of SAEs is that they do not require any charging process, and Yamane *et al.* have recently developed an SAE-based MEMS VEG.[13] The SAE is composed of polar organic molecules used for organic light-emitting diodes (OLEDs) such as tris-(8-hydroxyquinolinato)aluminum (Alq$_3$) and 1,3,5-tris(1-phenyl-1H-benzimidazol-2-yl)benzene (TPBi) [Figs. 1(d) and 1(e), respectively], where a molecular dipole spontaneously orders perpendicular to the substrate on average.[14–16] Thus, in the SAE, both positive and negative polarization charges exist on the film surface and reverse side as shown in Fig. 1(c). The key point is that the electric field is directed from the positive to negative polarization charges and will not be formed outside of the SAE. Therefore, in the SAE-VEG, the apparent driving force inducing charges on the vibrational electrode is unclear.

The operation of conventional E-VEG devices has been discussed since Winder and Kaufman proposed the concept of the electrostatic generator[17] and Matthew experimentally demonstrated a practical rotating-type generator.[18] In 1978, Jefimenko and Walker developed an electrostatic current generator having a disk electret and theoretically characterized its operation,[19] and the model and structure were refined by Tada.[20,21] After that, Boland *et al*. realized a micromachined rotational electret power generator and derived an output power as an intuitively understandable expression,[22] and later, Bartsch *et al*. extended the model to take parasitic capacitances into account.[23] Although the analytical model of E-VEGs has been gradually improved, the fundamental difference in the generated current (J_g) between the two types of electrets, namely, the unipolar type [Fig. 1(b)] and dipolar type [Fig. 1(c)], has not been understood in depth. Recently, Yang *et al*. have suggested that the electrical field distribution of an E-VEG with a dipolar electret is numerically identical to that of an E-VEG with a unipolar electret.[24] However, the experimental confirmation was not sufficient; they did not evaluate the relationship between the dipolar electret's surface potential (V_{sp}) and J_g in the device. In general, V_{sp} of a dipolar electret should increase linearly with the film thickness if constant polarization charges exist on the top and bottom surfaces of the electret. Thus, to clarify the operation mechanism of the dipolar electret-based VEG, it is essential to precisely control the thickness of the electret and measure J_g at each V_{sp}.

An SAE is classified as a dipolar electret and has the characteristic that V_{sp} linearly increases with the film thickness.[14] This is useful for evaluating the V_{sp} dependence of J_g, resulting in an understanding of the operation mechanism of not only SAE-VEGs but also conventional dipolar electret-based VEGs. In this study, the relationship between V_{sp} of the SAE and the root-mean-square value of J_g (J_{gr}) in the SAE-VEG was carefully examined by constructing an experimental system that can evaluate them both under the same conditions [Fig. 1(f)]. V_{sp} was precisely controlled by changing the film thickness. We experimentally demonstrated that J_{gr} in the SAE-VEG linearly increases with V_{sp} of the SAE, and developed a simple model for explaining the $J_{gr} \propto V_{sp}$ relationship. This result suggests that the output current of an SAE-VEG could be easily enhanced simply by increasing the thickness of the SAE.

2.   Materials and Methods

TPBi (sublimed, purity > 99.5%) was purchased from Luminescence Technology Corp. and Alq$_3$ (device grade) was supplied by Nippon Steel & Sumikin Chemical Co., Ltd. Both were vacuum-deposited with a base pressure of approximately 4×10^{-4} Pa. The deposition rate was set to 0.2 Å/s. V_{sp} was measured using the Kelvin probe (UHVKP020, KP Technology) in the vacuum chamber, which was directly connected to the evaporation chamber. A current/voltage amplifier (SR570, SRS) and an oscilloscope (TDS2001C, Tektronix) were used to measure J_g as shown in Fig. 1(f). In SAE film, V_{sp} disappears on light irradiation during or after film deposition.[16] This occurs because photo-generated electrons and holes compensate for polarization charges.[12] To avoid this depolarization, the film preparation and measurements were performed under dark and vacuum conditions.

3.   Model

Figure 2(a) shows an energy diagram of the SAE-VEG in the case that the vibrational and fixed electrodes are electrically connected. Here, E_{vac} and E_f indicate the vacuum and Fermi levels, respectively. Φ_{fix} and Φ_{vib} denote the work functions of the fixed and vibrational electrodes, respectively, and $\Delta\Phi$ is work function difference ($\Delta\Phi = \Phi_{fix} - \Phi_{vib}$). e and ε_0 are the elementary charge and the permittivity of the vacuum, and l_{sae} and l_{gap} indicate the film thickness of the SAE and the distance between the SAE surface and the vibrational electrode, respectively. V_{sp} is the surface potential of the film with respect to the fixed electrode. V_{gap} is the potential at the surface of the vibrational electrode with respect to the SAE surface ($eV_{gap} = \Delta\Phi - eV_{sp}$). In the case of the potential distribution shown in Fig. 2(a), εV_{gap} is negative because $\Delta\Phi < eV_{sp}$. By applying Gauss's law at the surface of the vibrational electrode, the induced charge density (σ_0) is given by $\sigma_0 = \varepsilon_0 \left(V_{gap}/l_{gap}\right)$. Thus, we obtain
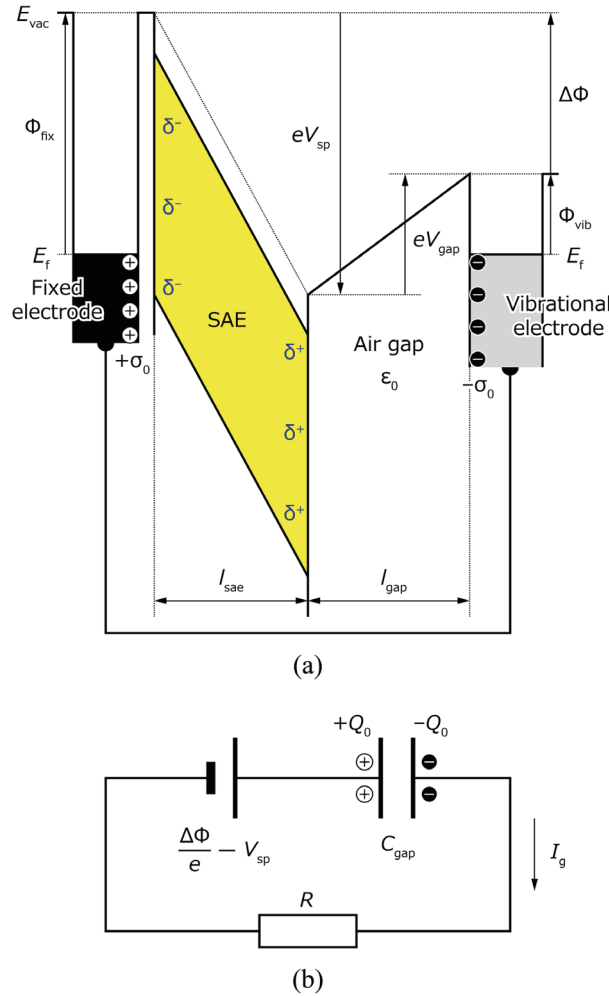

Fig. 2.   (Color online) (a) Energy diagram of SAE-based VEG in the case that the vibrational and fixed electrodes are electrically connected. (b) Equivalent circuit of SAE-VEG with the load resistance.

$$\sigma_0 = \varepsilon_0 \frac{1}{l_{gap}} \left(\frac{\Delta\Phi}{e} - V_{sp} \right). \tag{1}$$

l_{gap} varies with time (t) during electrode vibration, and J_g under the short-circuit condition is expressed by the time differential of σ_0. Assuming that V_{sp} is constant during electrode vibration, J_g can be derived as

$$J_g = \varepsilon_0 \left(\frac{\Delta\Phi}{e} - V_{sp} \right) \frac{d}{dt} \frac{1}{l_{gap}(t)}. \tag{2}$$

Equation (2) suggests that J_g is (inversely) proportional to V_{sp}. Note here that J_g of Eq. (2) can be easily measured using the experimental setup shown in Fig. 1(f).

The total amount of charge of the device (Q_0) equals $\sigma_0 S$, where S is the active area of the device. Using Eq. (1), we obtain $Q_0 = C_{gap} (\Delta\Phi/e - V_{sp})$, where C_{gap} is the capacitance of the air gap ($C_{gap} = \varepsilon_0 S/l_{gap}$). Therefore an equivalent circuit of the SAE-VEG can be expressed using a simple capacitor circuit, as shown in Fig. 2(b), where R and I_g indicate the load resistance and generated current ($I_g = J_g S$), respectively. The circuit dynamics during electrode vibration can be obtained using Kirchhoff's law as follows:

$$\frac{\Delta\Phi}{e} - V_{sp} = \frac{Q_0(t)}{C_{gap}(t)} + R I_g(t). \tag{3}$$

Because $I_g = dQ_0/dt$, we obtain

$$\frac{dQ_0(t)}{dt} + \frac{1}{RC_{gap}(t)} \cdot Q_0(t) = \frac{1}{R} \left(\frac{\Delta\Phi}{e} - V_{sp} \right). \tag{4}$$

Equation (4) can be analytically solved as

$$Q_0(t) = \left\{ \frac{\frac{\Delta\Phi}{e} - V_{sp}}{R} \int_0^t e^{-t_{RC}(t)} dt + Q_0(0) \right\} e^{t_{RC}(t)}, \tag{5}$$

$$t_{RC}(t) = -\int_0^t \frac{1}{RC_{gap}(t)} dt, \tag{6}$$

where t_{RC} denotes the time variation of the time constant in the equivalent circuit. Equations (5) and (6) are helpful for estimating the optimized load resistance and maximum output power under impedance matching.

4.   Results and Discussion

4.1   Surface potential and generated current measurements

To investigate the relationship between V_{sp} and J_g [Eq. (2)], l_{sae} dependences were measured in Alq$_3$- and TPBi-based SAEs. Figure 3(a) shows the contact potential difference (V_{cpd}) as a function of l_{sae} in Alq$_3$, and the inset shows an enlarged view of the thin-film region ($l_{sae} \leq$ 20 nm). Here, V_{cpd} equals $V_{sp} - \Delta\Phi/e$: V_{sp} with respect to the fixed electrode can be obtained by subtracting V_{cpd} at $l_{sae} > 0$ nm from V_{cpd} at $l_{sae} = 0$ nm ($-\Delta\Phi/e = -281.5$ mV). The right vertical axis denotes V_{sp} obtained in this manner. In the case of $l_{sae} \geq 20$ nm, V_{sp} linearly increased with increasing l_{sae} and reached 1.8 V at 200 nm without using a charging process. This giant surface potential (GSP) originates from the spontaneous orientation of the permanent dipole of Alq$_3$, as discussed in depth in Ref. 14. Moreover, the constant electric field suggests that positive and negative polarization charges exist on the film surface and reverse sides, respectively. The surface charge density (σ_s) was estimated to be 0.3 mC/m^2 using a relative permittivity of 3.2[15] and a slope of 10.8 mV/nm [see the solid line in Fig. 3(a)]. In a previous report, σ_s of Alq$_3$ was estimated to be 1.1 mC/m^2,[15] which is comparable to that of a polymer-based electret after corona charging[25] and approximately 3.7 times larger than that estimated in this study. This difference originates from the difference in the fabrication process, especially the deposition rate, which will be reported elsewhere.[26]

It is important to note that, at $l_{sae} \leq 20$ nm, Vs_p linearly decreases with a slope of 13.7 mV/nm [see the solid line in the inset of Fig. 3(a)]. This result indicates that the polarity of the surface
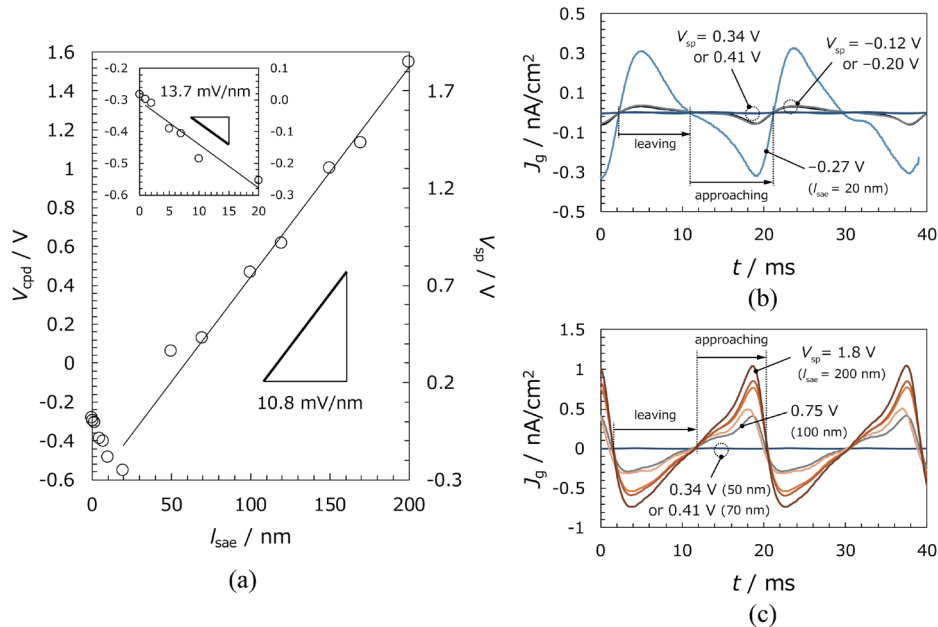

Fig. 3.   (Color online) (a) l_{sae} dependences of V_{cpd} (left vertical axis) and V_{sp} (right vertical axis) in Alq$_3$-SAE. The inset shows an enlarged view of the thin-film region (0 nm $\leq l_{sae} \leq$ 20 nm). (b), (c) Time dependences of J_g of Alq$_3$-VEG for 7 nm $\leq l_{sae} \leq$ 70 nm and 70 nm $\leq l_{sae} \leq$ 200 nm, respectively. The inset in Fig. 3(a) shows an enlarged view of the thin-film region (0 nm $\leq$ lsae $\leq$ 20 nm).

charge is negative in this thickness range, implying the opposite orientation of Alq_3, in complete contrast from previous reports.[14–16] We also found that the polarity is related to the amount of deposition during the KP measurements. Clarification of the polarity change will enable understanding of the mechanism of spontaneous orientation; however, this is beyond the scope of this article and will be discussed in a separate paper. The notable points for clarifying the relationship between V_{sp} and J_g are that (i) at $l_{sae} \leq 20$ nm, V_{sp} is negative and decreases linearly with increasing l_{sae} and (ii) V_{sp} is positive and increases linearly at $l_{sae} \geq 20$ nm.

In addition to the Alq_3-based samples, V_{sp} and J_g are enhanced with increasing l_{sae} in the TPBi-based sample as shown in Figs. 4(a) and 4(b), respectively. This result clearly suggests that J_g can be controlled by changing l_{sae} in SAE-based VEGs at $l_{sae} \geq 20$ nm. V_{sp} of TPBi at $l_{sae} < 20$ nm is, on the contrary, almost constant around 0.1 V [inset in Fig. 4(a)]. It may be that V_{sp} depends on the deposition conditions, similarly to V_{sp} of Alq_3 [Fig. 3(a)], although the possibility of some effect of the substrate on V_{sp} cannot be ignored at this stage.

4.2   Relationship between surface potential and generated current

As shown in Figs. 3(c) and 4(b), J_g increases with l_{sae} except in the thin-film region, suggesting that J_g depends on V_{sp}. To examine the relationship, J_{gr} in the Alq_3-VEG is estimated from Fig. 3(c) and compared with V_{sp}. Figure 5(a) shows the V_{sp} dependence of J_{gr}, indicating that J_{gr} is almost proportional to V_{sp} of Alq_3. Furthermore, this linear relationship was also observed in a TPBi-based VEG as shown in Fig. 5(b). These results indicate that Eq. (2) is valid and that the $J_{gr} \propto V_{sp}$ relationship is maintained. In other words, J_g of the SAE-VEG can be easily enhanced simply by increasing the film thickness. This guideline is simple but essential to realize an SAE-based VEG with high output power.

Finally, a close look at Figs. 3(b) and 3(c) reveals that the polarity of J_g changes: at $l_{sae} \geq 100$ nm, J_g becomes negative and positive when the electrode moves away from and
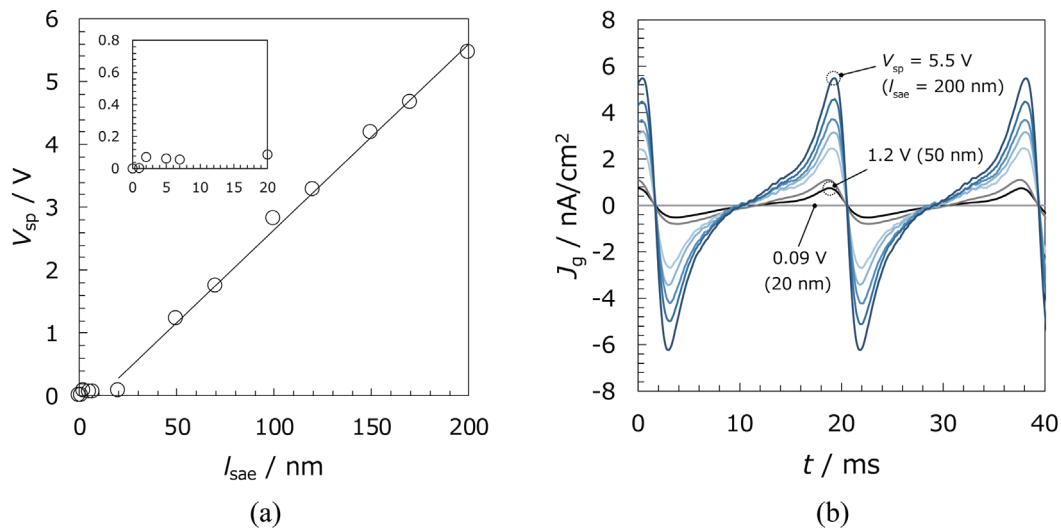

Fig. 4.   (Color online) (a) l_{sae} dependence of V_{sp} in TPBi-based SAE, (b) l_{sae} dependence of J_g in TPBi-based VEG.
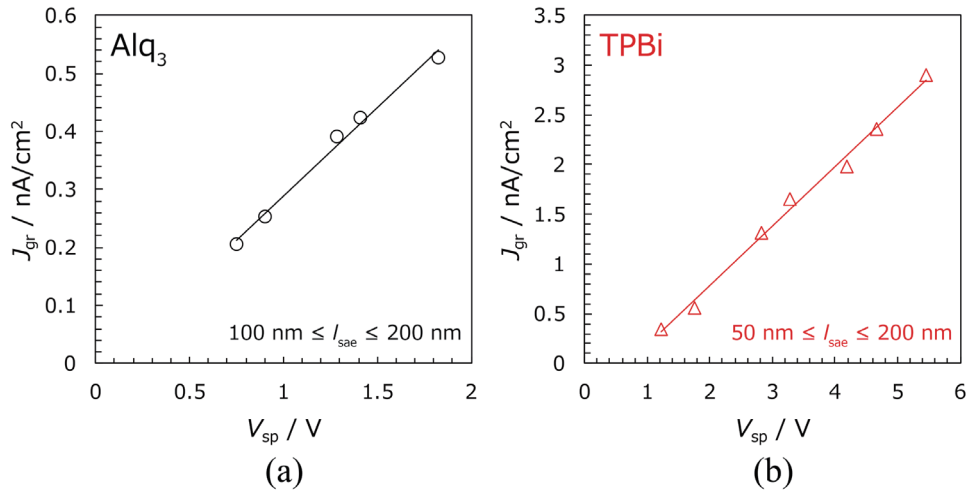
Fig. 5.   (Color online) V_{sp} dependence of J_{gr} in (a) Alq$_3$-based and (b) TPBi-based VEGs.

approaches the Alq$_3$ surface, respectively. On the other hand, J_g at l_{sae} = 20 nm shows positive and negative values as the electrode leaves and approaches, respectively. This change can be explained by the polarity change of the $\Delta\Phi/\varepsilon - V_{sp}$ term in Eq. (2), which changes from positive to negative when V_{sp} is larger than $\Delta\Phi/\varepsilon$. This result also supports the conclusion that Eq. (2) is valid for the SAE-VEG. Thus, we conclude that, in the SAE-VEG, charges on the vibrational electrode are induced by V_{sp} of the SAE in accordance with Eq. (1).

5.   Conclusions

To clarify the current generation mechanism in an SAE-VEG during electrode vibration, the relationship between V_{sp} of the SAE and J_{gr} in the SAE-VEG was precisely examined by developing a measurement system that can evaluate both of them under the same conditions. J_{gr} in the SAE-VEG increased proportionally to V_{sp} of the SAE according to the proposed model, suggesting that the electric field of the SAE induces the charges on the vibrational electrode. These results demonstrate that the output current of SAE-VEGs is easily enhanced by increasing the film thickness of the SAE.

To understand the device physics of SAE-VEGs in more detail, it is important to study whether the waveform of J_g (Eq. (2)) corresponds to the experimental results of Figs. 3(b), 3(c), and 4(b). Then, the equivalent circuit in Fig. 2(b) and Eqs. (5) and (6) can be used to estimate the maximum output power and optimized resistance of the device. Related research is ongoing. We believe that a high-output-power and easy-to-fabricate E-VEG can be realized by constructing an appropriate device structure for the SAE.

References

1 H. Akinaga: Jpn. J. Appl. Phys. **59** (2020) 110201. https://doi.org/10.35848/1347-4065/abbfa0
2 Y. Suzuki: IEEJ Trans. **6** (2011) 101. https://doi.org/10.1002/tee.20631
3 S. P. Beeby, M. J. Tudor, and N. M. White: Meas. Sci. Technol. **17** (2006) R175. https://doi.org/10.1088/0957-0233/17/12/R01
4 S. Roundy, P. K. Wright, and J. Rabaey: Comput. Commun. **26** (2003) 1131. https://doi.org/10.1016/S0140-3664(02)00248-7
5 Y. Suzuki, D. Miki, M. Edamoto, and M. Honzumi: J. Micromech. Microeng. **20** (2010) 104002. https://doi.org/10.1088/0960-1317/20/10/104002
6 G. M. Sessler: Electrets (Laplacian Press, 1998) 3rd ed.
7 K. Hagiwara, M. Goto, Y. Iguchi, T. Tajima, Y. Yasuno, H. Kodama, K. Kidokoro, and Y. Suzuki: IEEE Dielectr. Electr. Insul. **19** (2012) 1291. https://doi.org/10.1109/TDEI.2012.6260003
8 K. Hagiwara, M. Goto, Y. Iguchi, Y. Yasuno, H. Kodama, K. Kidokoro, and T. Tajima: Appl. Phys. Express **3** (2010) 091502. https://doi.org/10.1143/APEX.3.091502
9 G. Hashiguchi, D. Nakasone, T. Sugiyama, M. Ataka, and H. Toshiyoshi: AIP Adv. **6** (2016) 035004. https://doi.org/10.1063/1.4943528
10 T. Sugiyama, M. Aoyama, Y. Shibata, M. Suzuki, T. Konno, M. Ataka, H. Fujita, and G. Hashiguchi: Appl. Phys. Express **4** (2011) 114103. https://doi.org/10.1143/APEX.4.114103
11 U. Mescheder, B. Müller, S. Baborie, and P. Urbanovic: J. Micromech. Microeng. **19** (2009) 094003. https://doi.org/10.1088/0960-1317/19/9/094003
12 Y. Tanaka, N. Matsuura, and H. Ishii: Sci. Rep. **10** (2020) 6648. https://doi.org/10.1038/s41598-020-63484-9
13 D. Yamane, H. Kayaguchi, K. Kawashima, H. Ishii, and Y. Tanaka: Appl. Phys. Lett. **119** (2021) 254102. https://doi.org/10.1063/5.0072596
14 Y. Noguchi, W. Brütting, and H. Ishii: Jpn. J. Appl. Phys. **58** (2019) SF0801. https://doi.org/10.7567/1347-4065/ab0de8
15 Y. Noguchi, Y. Miyazaki, Y. Tanaka, N. Sato, Y. Nakayama, T. D. Schmidt, W. Brütting, and H. Ishii: J. Appl. Phys. **111** (2012) 114508. https://doi.org/10.1063/1.4724349
16 E. Ito, Y. Washizu, N. Hayashi, H. Ishii, N. Matsuie, K. Tsuboi, Y. Ouchi, Y. Harima, K. Yamashita, and K. Seki: J. Appl. Phys. **92** (2002) 7306. https://doi.org/10.1063/1.1518759
17 H. H. Winder and S. Kaufman: Electr. Eng. **72** (1953) 511. https://doi.org/10.1109/EE.1953.6438064
18 R. E. Matthew: Electr. Eng. **81** (1962) 850. https://doi.org/10.1109/EE.1962.6446580
19 O. D. Jefimenko and D. K. Walker: IEEE Trans. Ind. Appl. **IA-14** (1978) 537. https://doi.org/10.1109/TIA.1978.4503588
20 Y. Tada: IEEE Trans. Elect. Insul. **EI-21** (1986) 457. https://doi.org/10.1109/TEI.1986.349093
21 Y. Tada: Jpn. J. Appl. Phys. **31** (1992) 846. https://doi.org/10.1143/JJAP.31.846
22 J. Boland, Y.-H. Chao, Y. Suzuki, and Y. C. Tai: The 16th Annu. Int. Conf. Micro Electro Mech. Syst. (2003) 538. https://doi.org/10.1109/MEMSYS.2003.1189805
23 U. Bartsch, J. Gaspar, and O. Pail: J. Micromech. Microeng. **20** (2010) 035016. https://doi.org/10.1088/0960-1317/20/3/035016
24 Z. Yang, L. Tang, K. Tao, and K. C. Aw: Int. J. Precis. Eng. Manuf.-Green Technol. **8** (2019) 113. https://doi.org/10.1007/s40684-019-00156-8
25 K. Kashiwagi, K. Okano, T. Miyajima, Y. Sera, N. Tanabe, Y. Morizawa, and Y. Suzuki: J. Micromech. Microeng. **21** (2011) 125016. https://doi.org/10.1088/0960-1317/21/12/125016
26 Y. Tanaka, N. Matsuura, and H. Ishii: Tech. Dig. Manuscr. in PowerMEMS (2019) 1. https://doi.org/10.1109/PowerMEMS49317.2019.41031605688